Correlation between structural and low-temperature thermoelectric properties of $Zn_{13+x}Sb_{10}$ compounds

Go Nakamoto,[a] Keisuke Kinoshita, and Makio Kurisu
Japan Advanced Institute of Science and Technology, Nomi, Ishikawa 923-1292, Japan

(Received 6 April 2008; accepted 4 November 2008; published online 14 January 2009)

Structural, metallurgical, and low-temperature thermoelectric properties have been investigated for $Zn_{13+x}Sb_{10}$ compounds prepared by the gradient freeze and vacuum melt-quench methods at various starting Zn compositions. The Rietveld analysis of the powder x-ray diffraction profiles indicates that the excess Zn occupies mainly the 36*f*-3 and 36*f*-4 interstitial sites. It is also revealed that the actual Zn composition and lattice constants have strong correlation with occupation factors of the 36*f*-3 and 36*f*-4 sites. The thermoelectric property strongly depends on the actual Zn composition. The enhancement in the electrical resistivity and Seebeck coefficient associated with the β to α structural phase transition is more remarkable for the samples with larger starting Zn composition. On the other hand, the lattice thermal conductivity also exhibits a remarkable increase at the transition temperature, indicating an ordered Zn structure in the α phase. These facts indicate that the occupation of Zn in the two interstitial 36*f*-3 and 36*f*-4 sites gives a significant effect on the crystal and electronic structures of the $Zn_{13+x}Sb_{10}$ system. © *2009 American Institute of Physics*. [DOI: 10.1063/1.3043884]

I. INTRODUCTION

The β-$Zn_{13}Sb_{10}$ compound which has been well known as Zn_4Sb_3 until the early 2000s has attracted much attention as one of the prime candidates for practical thermoelectric application in the moderate temperature range because of the high thermoelectric performance, $ZT=1.3$ at 670 K.[1,2] The 13:10 compound possesses many structural phases: γ' ($766\ \mathrm{K} \leq T \leq 837\ \mathrm{K}$), γ ($766\ \mathrm{K} \leq T \leq 795\ \mathrm{K}$), β ($265\ \mathrm{K} \leq T \leq 766\ \mathrm{K}$), α ($235\ \mathrm{K} \leq T \leq 265\ \mathrm{K}$), and α' ($T \leq 235\ \mathrm{K}$). Main concerns have been in the β-phase physical properties. However, there have been many mysterious problems left about the crystal structures of the compound. Mayer *et al.* first proposed the crystal structure of the β phase.[3] In the past few years, many efforts have been devoted in determining the crystal structure and actual chemical composition of the 13:10 compound.[4–12] Snyder *et al.* determined the detailed crystal structure of the β phase.[7] They revealed that the extra interstitial sites occupied by Zn atoms exist and claimed that the disordered structure of Zn atoms leads to the extremely low thermal conductivity in the β phase. The actual Zn composition has been determined to be 56.52 at. % Zn (13:10) which is smaller than 57.14 at. % Zn (4:3) by Mayer *et al.* Quite recently, Schweika *et al.* suggested that dumbbell rattling of Sb dimers along the *c* axis plays an important role in realizing the extremely low thermal conductivity.[13]

Furthermore, the crystal structure of the low-temperature α phase has been investigated by many groups.[6,8–10] Nylén *et al.* proposed that the α phase crystallizes in the monoclinic structure which is formed by slight distortion of the β phase and has an ordered Zn structure.[9] It should be noted that the number of Zn atoms increases, associated with the β to α structural phase transition, and the ideal composition is claimed to be 56.52 at. % Zn (13:10) in the α phase. They have also calculated the electronic band structures of the α and β phases based on the determined crystal structures. According to the calculation, the Fermi level shifts to near the conduction band edge in the α phase when the number of Zn atoms is increased, resulting in the decrease in carrier (hole) concentration. More recently, a second low-temperature phase (α' phase) has been detected below 235 K.[14,15]

The thermoelectric properties at low temperature have also been investigated intensively.[16–24] Nakamoto *et al.* found that the transport properties in the α phase are strongly dependent on the starting Zn composition.[19,23] Furthermore, it should be noted that the low-temperature thermoelectric property depends largely on the sample preparation conditions such as starting chemical composition and preparation method.

In the present study, in order to clarify the correlation between the structural and low-temperature thermoelectric properties of the $Zn_{13}Sb_{10}$ compound, we have performed crystal structure refinement and thermoelectric measurements for four $Zn_{13+x}Sb_{10}$ compounds with various starting compositions ranging from 56.52 (13:10) to 60.00 (3:2) at. % Zn prepared by the gradient freeze (GF) and vacuum melt-quench (VMQ) methods.

II. EXPERIMENTAL

Four $Zn_{13+x}Sb_{10}$ samples were prepared at the four different starting compositions: by a GF method for 56.52 (13:10), 57.14 (4:3), and 59.00 at. % Zn and a VMQ method for 60.00(3:2) at. % Zn, as listed in Table I. The constituent elements of Zn (6N) and Sb (6N) were loaded into a double quartz tube and sealed under vacuum down to 10^{-5} Torr. In the case of the GF method, the elements were melted at 1023 K for 3 h in a vertical GF furnace and the crystals were grown at a rate of 0.3 mm/h in the temperature gradient of 40

[a]Author to whom correspondence should be addressed. Electronic mail: gou@jaist.ac.jp. Tel.: +81-761-51-1543. FAX: +81-761-51-1149.

TABLE I. $Zn_{13+x}Sb_{10}$ samples prepared in this study.

Sample name	Preparation method	Starting Zn composition (at. % Zn)
56.52 GF	Gradient freeze	56.52 [13:10]
57.14 GF	Gradient freeze	57.14 [4:3]
59.00 GF	Gradient freeze	59.00
60.00 VMQ	Vacuum melt quench	60.00 [3:2]

K/cm at the solid-liquid interface. For the VMQ method, the elements were melted at 1023 K for 3 days and then quenched into ice water. The grown ingots were cut into several pieces with suitable shapes for various physical measurements using a spark erosion cutter (SANKYO Eng. Ltd., DE-60). Then, the surface of the pieces was polished by an emiry paper.

The polished surface of the pieces was observed by an optical polarizing microscope (OLYMPUS, BX60). The powder x-ray diffraction (XRD) measurement was performed at room temperature (in the β phase) by a Rigaku RINT-2000 using Cu $K\alpha$ radiation. The powder XRD profiles were analyzed to determine the crystallographic parameters by the Rietveld method using a pattern profile fitting program, RIETAN-2000.[25] Electron-probe microanalysis (EPMA) was also performed to examine the spatial distribution of the composition of the β phase using a JEOL JXA-8621. The samples for EPMA were polished by fine alumina powder to make the surface flat and clean. The electrical resistivity, Seebeck coefficient, and thermal conductivity measurements were carried out by a physical property measurement system (Quantum Design Ltd.) in the temperature range between 5 and 340 K for the rectangular parallel piped specimens with the dimension of $2\times2\times4$ mm^3 along the crystal growth direction cut from the bottom part of the ingots.

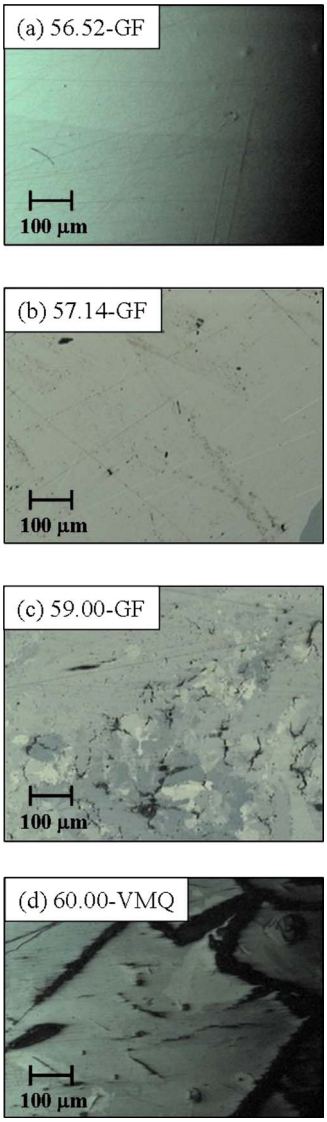

FIG. 1. (Color online) Morphology of the surface for (a) 56.52 GF, (b) 57.14 GF, (c) 59.00 GF, and (d) 60.00 VMQ observed by an optical polarizing microscope.

III. RESULTS AND DISCUSSION

A. Sample characterization

1. Metallurgical observation

Figure 1 shows the surface morphology for all the samples. In the sample with the starting composition 13:10 (56.52 at. % Zn), any segregated impurity phases are not observed in the matrix. The grain size is found to be as large as 1×1 mm^2. With increasing the starting Zn composition, it decreases. The fine grain structure observed in the samples with greater starting Zn composition is attributed to the eutectic reaction between the 13:10 and 3:2 phases in the solidification process.[5] The 60.00-VMQ sample has many cracks due to the rapid quenching process for the ingot preparation.

2. Rietveld analysis of powder x-ray diffraction profiles

Figure 2 shows the powder XRD profiles and results of the Rietveld refinement at 300 K for all the samples prepared at the different Zn starting compositions of (a) 56.52 (13:10), (b) 57.14 (4:3), (c) 59.00, and (d) 60.00(3:2) at. % Zn. The Reitveld analysis was performed based on the structural model proposed by Snyder *et al.*[7] The sample with the stoichiometric starting composition, 13:10, is found to be of single phase. Zn metal segregates as an impurity phase in the ingots with the higher Zn starting composition except for the 4:3 ingot. The small amount of the ZnSb phase is found as an impurity phase in the 4:3 sample. The amount of the impurity Zn metal is larger for the samples with larger Zn starting composition as listed in Table II.

The actual Zn composition and lattice constants determined by the Rietveld analysis are listed in Table II. For the actual Zn compositions of the three GF samples, one cannot find greater difference than 0.3 at. % Zn. The distribution of the composition in the GF samples is in good agreement with the previous result by EPMA.[11] The GF samples are grown in a thermally equilibrium condition. Therefore, it is supposed that the larger amount of the excess Zn is wiped out to the top part of the ingots during the crystal growth. In fact, the amount of the Zn impurity phase is larger for the samples with larger starting Zn composition. In contrast, the VMQ

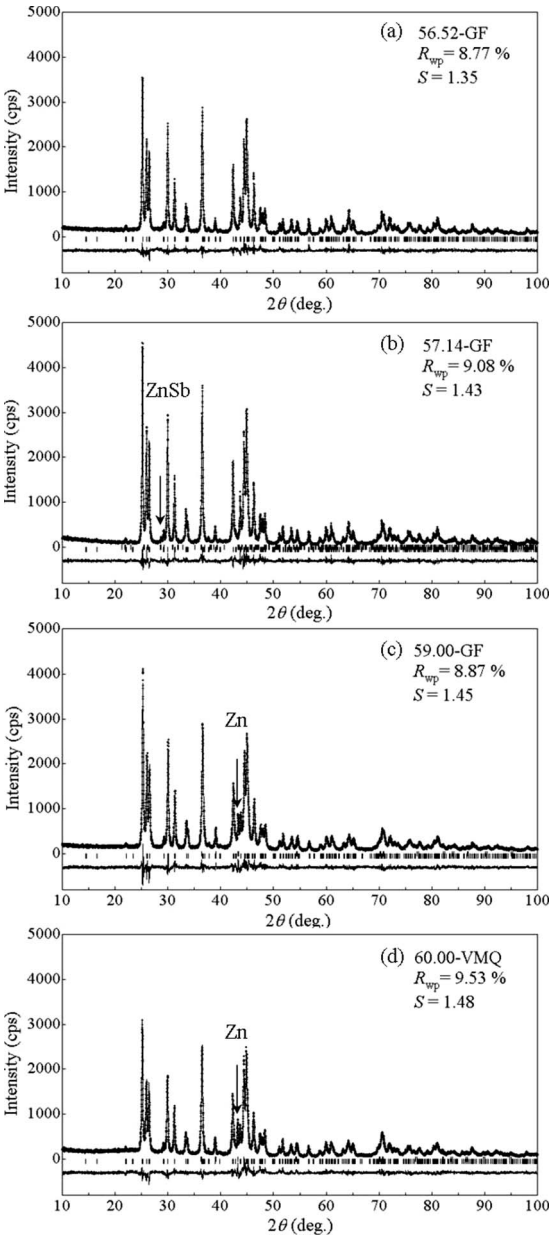

FIG. 2. Powder XRD profiles and the results of the Rietveld analysis for $Zn_{13+x}Sb_{10}$ samples with (a) 56.52, (b) 57.14, (c) 59.00, and (d) 60.00 at. % Zn.

sample has larger actual Zn composition by 2 at. % Zn than the GF ingots. The lattice constants are also larger in the VMQ sample than in the GF ones, reflecting the larger Zn composition in the ingots.

TABLE II. Actual Zn composition, lattice constants, and impurity phases determined by the Rietveld analysis.

Sample name	Actual Zn composition (at. % Zn)	a (Å)	c (Å)	Impurity phases (wt. %)
56.52 GF	56.70	12.2279(3)	12.4190(2)	···
57.14 GF	56.96	12.2298(3)	12.4235(2)	ZnSb (1.9)
59.00 GF	56.90	12.2122(4)	12.4045(3)	Zn (6.0)
60.00 VMQ	58.71	12.2422(4)	12.4370(3)	Zn (6.6)

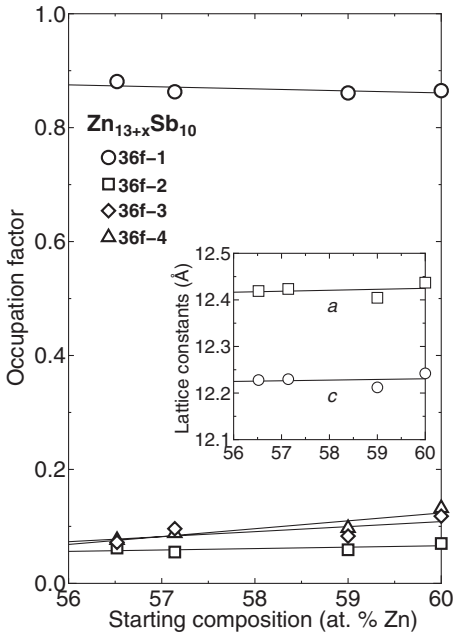

FIG. 3. Occupation factors at four interstitial Zn sites, 36*f*-1, 36*f*-2, 36*f*-3, and 36*f*-4 as a function of starting Zn composition. The inset shows the lattice constants as a function of starting Zn composition.

The occupation factors of the four Zn sites (36*f*-1, 36*f*-2, 36*f*-3, and 36*f*-4) are shown in Fig. 3 as a function of the starting Zn composition. Most of Zn atoms occupy the 36*f*-1 site with the occupation factor of about 0.9. It is particularly interesting to note that the two interstitial sites of 36*f*-3 and 36*f*-4 can accommodate more Zn atoms when the starting Zn composition is increased. For the 36*f*-3 site, the occupation factor is increased from 0.07 to 0.12. On the other hand, the 36*f*-1 site, where 90% of the total Zn atoms occupy, shows a decrease in occupation factor. Thus, the excess Zn is mainly introduced into these two interstitial sites, 36*f*-3 and 36*f*-4. Actually, the VMQ sample has larger lattice constants than the GF ones as shown in the inset of Fig. 3. The strong correlation is concluded between the lattice constants and occupation factors of the 36*f*-3 and 36*f*-4 sites.

Figures 4(a)–4(d) represent the four Zn sites of the 36*f*-1, 36*f*-2, 36*f*-3, and 36*f*-4, respectively, projected onto the hexagonal basal plane. The Zn atoms at the 36*f*-1 and 36*f*-2 form triangles surrounding the Sb2 sites. On the other hand, the Zn atoms at the 36*f*-3 and 36*f*-4 surround the Sb2 sites by hexagonal rings. It is, therefore, expected that the increase in occupation factors of the 36*f*-3 and 36*f*-4 sites influences appreciably the electronic band structure of $Zn_{13+x}Sb_{10}$.

3. Electron-probe microanalysis

The spatial distribution of the Zn composition is shown in Fig. 5 for the ingots prepared at 57.14 at. % Zn (4:3, GF) and 60.00 at. % (3:2, VMQ). The analysis was performed along the central axis of the cylindrical ingots. The Zn concentration is constant along the crystal growth direction z. Such a uniform distribution has been reported for the GF sample at 57.14 at. % Zn.[11] Scattering in Zn concentration

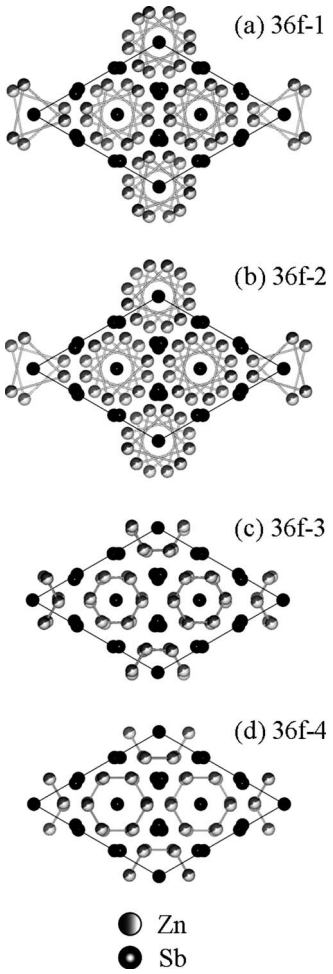

FIG. 4. Crystal structure of β-$Zn_{13}Sb_{10}$ projected onto the hexagonal basal plane for (a) 36*f*-1, (b) 36*f*-2, (c) 36*f*-3, and (d) 36*f*-4 sites.

observed at smaller z is attributed to the existence of cracks. On the other hand, the 3:2 VMQ sample exhibits relatively larger scattering in the composition throughout the ingot due to the cracks introduced by rapid quenching process. It should be also noted that the 3:2 VMQ sample has larger actual Zn composition than the 4:3 GF sample by 2 at. % Zn. The difference in chemical composition between these two samples is consistent with that determined by the Rietveld analysis.

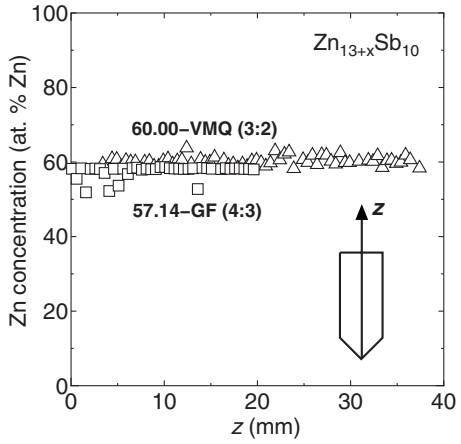

FIG. 5. Spatial distribution of the actual Zn composition along the crystal growth direction determined by EPMA for 57.14 GF and 60.00 VMQ samples.

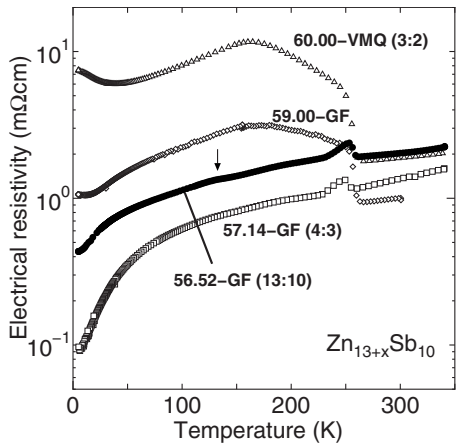

FIG. 6. Electrical resistivity as a function of temperature for $Zn_{13+x}Sb_{10}$ samples prepared at various starting compositions.

B. Thermoelectric property

1. Electrical resistivity

Figure 6 shows the electrical resistivity ρ as a function of temperature for all the samples. The samples with 13:10 and 4:3 starting compositions exhibit an increase in ρ associated with the β to α structural phase transition at T_s=260 K, indicating smaller carrier concentration in the α phase. ρ takes a maximum around 250 K and then shows a kink at 235 K, corresponding to the α to α' phase transition. It should be noted that another phase transition is signaled by a small anomaly indicated by an arrow at 130 K only in the 56.52 GF sample.

In contrast, ρ of the 59.00 GF and 60.00 VMQ samples is enhanced remarkably at the β to α phase transition. Furthermore, the transition temperature T_s is shifted to higher temperature from 260 to 265 K. ρ of the 60.00 VMQ sample changes greatly the slope at 250 K, shows a broad maximum around 160 K, and then upturns below 30 K. Such a temperature dependence of ρ implies smaller carrier concentration in the α phase. Any anomalies are not found at 235 K (α to α' transition) and 130 K in the 60.00 VMQ sample.

2. Seebeck coefficient

The temperature dependence of the Seebeck coefficient $S(T)$ is displayed for all the samples in Fig. 7. The close correlation is found between $S(T)$ and $\rho(T)$. One can find that the 13:10 sample has the largest S of 150 μV/K at 340 K. The samples with larger starting Zn composition show more remarkable enhancement in S at T_s. Thus, the enhancement of S at T_s is attributed to the reduction in carrier concentration. In fact, hole concentration is decreased, associated with the β to α transition by one order of magnitude.[18] Furthermore, the electronic band calculation by Nylén *et al.* demonstrated that hole concentration is reduced by increase in number of electrons associated with the β to α, disorder to order structural transition.[9] It is interesting to note that the samples prepared at larger starting Zn compositions show larger en-

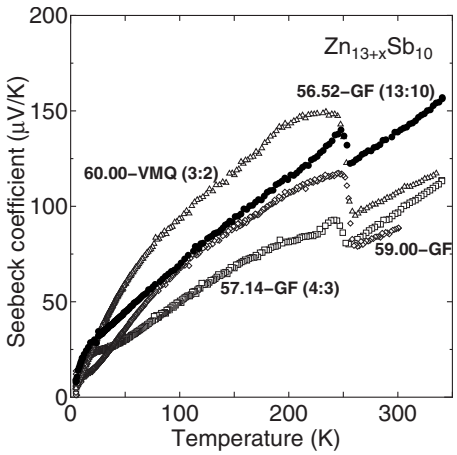

FIG. 7. Seebeck coefficient as a function of temperature for $Zn_{13+x}Sb_{10}$ samples prepared at various starting compositions.

hancement in ρ and S at T_s. This suggests that the Zn atoms accommodated in the 36*f*-3 and 36*f*-4 sites play an important role for the β to α structural phase transition. Since the number of Zn atoms is larger in the α phase, it is supposed that the β to α structural phase transition takes place more completely in the samples with larger Zn composition.

3. Thermal conductivity

The thermal conductivity κ is displayed as a function of temperature in Fig. 8. All the samples show a peak in the $\kappa(T)$ at 15 K. The sample of 59.00 at. % Zn has larger peak value than others because of the relatively large amount of metallic Zn impurity phase involved. The smallest peak value in the 60.00 VMQ sample is due to the larger amount of cracks introduced by the quenching process.

The anomaly associated with the β to α structural phase transition also appears in the $\kappa(T)$ for all the samples. The inset shows the lattice thermal conductivity κ_L estimated by assuming the Wiedemann–Franz law around T_s. κ_L is appreciably enhanced at T_s with lowering temperature. Since ρ of all the samples increases at T_s, the increase in κ is attributed to the enhancement of the lattice contribution to the total

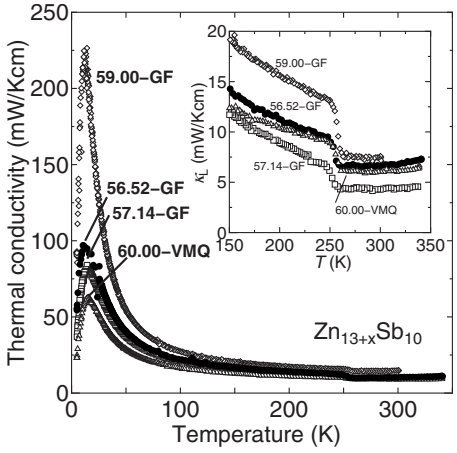

FIG. 8. Thermal conductivity as a function of temperature for $Zn_{13+x}Sb_{10}$ samples prepared at various starting compositions. The inset shows the lattice thermal conductivity as a function of temperature around the β to α structural transition temperature.

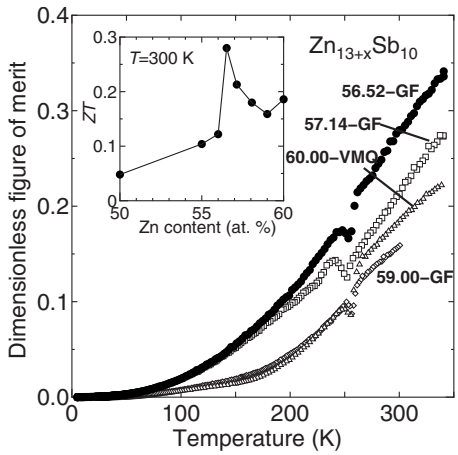

FIG. 9. Dimensionless figure of merit as a function of temperature for $Zn_{13+x}Sb_{10}$ samples prepared at various starting compositions. The inset shows dimensionless figure of merit at 300 K as a function of Zn content. The solid line is a guide for the eyes.

thermal conduction. Such an enhancement of the lattice thermal conductivity is attributed to the ordered structure of the α phase.[9] The samples with larger Zn composition exhibit larger enhancement in κ_L at T_s. This fact also supports more complete structural phase transition in the samples with larger Zn composition.

4. Dimensionless figure of merit

Figure 9 shows the temperature dependence of the dimensionless figure of merit ZT for all the samples. The 13:10 sample has greater thermoelectric performance with $ZT = 0.35$ at 340 K. The inset shows the ZT at 300 K as a function of the starting Zn composition. The ZT values obtained in the previous study for the samples with other starting compositions[19] are also plotted in this figure. It is shown that ZT has a maximum at a stoichiometric composition, 56.52 at. % Zn (13:10).

IV. CONCLUSION

The structural, metallurgical, and thermoelectric properties have been investigated for the $Zn_{13+x}Sb_{10}$ compounds prepared by the GF and VMQ methods to examine the correlation between the structural and low-temperature thermoelectric properties of $Zn_{13}Sb_{10}$ compound. We conclude as follows.

(1) It is revealed that the actual Zn composition and lattice constants have a strong correlation with the occupation factor of the 36*f*-3 and 36*f*-4 sites for $Zn_{13+x}Sb_{10}$. It is indicated that the excess Zn is introduced mainly into these two interstitial Zn sites, 36*f*-3 and 36*f*-4.

(2) The thermoelectric properties strongly depend on the Zn composition. The samples prepared at larger starting Zn composition show larger enhancement in the electrical resistivity and Seebeck coefficient associated with the β to α structural phase transition. This indicates that the Zn atoms at the 36*f*-3 and 36*f*-4 sites play an important role for the structural phase transition. The lattice thermal conductivity exhibits a remarkable increase at T_s,

indicating an ordered structure of the α phase. These facts indicate that the Zn occupation in the two interstitial sites, 36*f*-3 and 36*f*-4, gives a strong influence on the electronic and crystal structures both in the α and β phases of the $Zn_{13+x}Sb_{10}$ system.

(3) The 13:10 sample shows the best thermoelectric performance both in the β and α phases. The dimensionless figure of merit *ZT* has the largest value of 0.35 at 340 K. This result indicates that the precise control of Zn composition is very important in optimizing the thermoelectric performance of the $Zn_{13}Sb_{10}$ compound.

[1]T. Caillat, J. P. Fleurial, and A. Borshchevsky, J. Phys. Chem. Solids **58**, 1119 (1997).
[2]T. Caillat, J. P. Fleurial, and A. Borshchevsky, Proceedings of the 15th International Conference on Thermoelectrics, 1996, p. 151.
[3]I. Mayer, I. Mikhail, and K. Schubert, J. Less Common Met. **59**, 19 (1972).
[4]V. Izard, M. C. Record, and J.C. Tedenac, J. Alloys Compd. **345**, 257 (2002).
[5]V. Izard and M. M. Record, CALPHAD: Comput. Coupling Phase Diagrams Thermochem. **25**, 567 (2002).
[6]T. Souma, G. Nakamoto, M. Kurisu, K. Kato, and M. Takata, Proceedings of the 21st International Conference on Thermoelectrics, 2003, p. 282.
[7]G. Snyder, M. Christensen, E. Nishibori, T. Caillat, and B. B. Iversen, Nature Mater. **3**, 458 (2004).
[8]F. Cargnoni, E. Nishibori, P. Rabiller, L. Bertini, G. J. Synder, M. Christensen, C. Gatti, and B. B. Iversen, Chem.-Eur. J. **10**, 3861 (2004).
[9]J. Nylén, M. Anderson, S. Lidin, and U. Häussermann, J. Am. Chem. Soc. **126**, 16306 (2004).
[10]A. S. Mikhaylushkin, J. Nylén, and U. Häussermann, Chem.-Eur. J. **11**, 4912 (2005).
[11]G. Nakamoto, N. Akai, M. Kurisu, I.-H. Kim, S.-C. Ur, and V. L. Kuznetsov, J. Alloys Compd. **432**, 116 (2007).
[12]G. Nakamoto, K. Kinoshita, and M. Kurisu, J. Alloys Compd. **436**, 65 (2007).
[13]W. Schweika, R. P. Hermann, M. Prager, J. Perßon, and V. Keppens, Phys. Rev. Lett. **99**, 125501 (2007).
[14]Y. Mozharivskyj, Y. Janssen, J. L. Harringa, A. Kracher, A. O. Tsokol, and G. J. Miller, Chem. Mater. **18**, 822 (2006).
[15]J. Nylén, S. Lidin, M. Anderson, B. B. Iversen, H. Liu, N. Newmann, and U. Häussermann, Chem. Mater. **19**, 834 (2007).
[16]T. Souma, G. Nakamoto, and M. Kurisu, Proceedings of the 20th International Conference on Thermoelectrics, 2002, p. 273.
[17]T. Souma, G. Nakamoto, and M. Kurisu, J. Alloys Compd. **340**, 275 (2002).
[18]T. Souma, G. Nakamoto, and M. Kurisu, Proceedings of the 21st International Conference on Thermoelectrics, 2003, p. 279.
[19]G. Nakamoto, N. Akai, and M. Kurisu, Proceedings of the 23rd International Conference on Thermoelectrics, 2004, p. 133.
[20]V. L. Kuznetsov and D. M. Rowe, J. Alloys Compd. **372**, 103 (2004).
[21]G. Nakamoto, T. Souma, M. Yamaba, and M. Kurisu, J. Alloys Compd. **377**, 59 (2004).
[22]J. B. Park, I.-H. Kim, T. W. Hong, S.-C. Ur, Y. G. Ryu, G. Nakamoto, and M. Kurisu, Mater. Sci. Forum **510–511**, 1070 (2006).
[23]G. Nakamoto, N. Akai, and M. Kurisu, J. Alloys Compd. **437**, 151 (2007).
[24]J. Nylén, S. Lidin, M. Anderson, H. Liu, N. Newmann, and U. Häussermann, J. Solid State Chem. **180**, 2603 (2007).
[25]F. Izumi and T. Ikeda, Mater. Sci. Forum **321–324**, 198 (2000).